

Explicit core-hole single-particle methods for L - and M -edge X-ray absorption and electron energy-loss spectra

Esther A. B. Johnsen,^{1,2} Naoki Horiuchi,^{1,2} Toma Susi,³ and Michael Walter^{1,2,4}

¹*Cluster of Excellence livMatS @ FIT*

²*FIT–Freiburg Center for Interactive Materials and Bioinspired Technologies, University of Freiburg, 79104 Freiburg, Germany*

³*University of Vienna, Faculty of Physics, Boltzmannngasse 5, 1090 Vienna, Austria*

⁴*Fraunhofer IWM, MikroTribologie Centrum μ TC, 79110 Freiburg, Germany.*

(*Electronic mail: esther.johnsen@livmats.uni-freiburg.de)

(Dated: 14 April 2025)

Single-particle methods based on Kohn-Sham unoccupied states to describe near-edge X-ray absorption (XAS) spectra are routinely applied for the description of K -edge spectra, as there is no complication due to spin-orbit (SO) coupling. L - and M -edge spectra are often addressed via variants of time-dependent density functional theory (TDDFT) based on SO calculations. Here, we present a computationally efficient implementation based on single-particle calculations with core holes within the frozen-core approximation. Combined with a semiempirical energy shift and a fixed spin-orbit splitting, this allows for a prediction of experimental spectra on the absolute energy scale. Such spectra are compared to linear-response TDDFT for molecules and show similar or even better match with experiment, except for multiplet effects that are not covered by the single-particle approximation. A similar picture emerges for solids, where good qualitative and sometimes even quantitative agreement to XAS and electron energy-loss spectra is achieved.

I. INTRODUCTION

X-ray absorption (XAS) is a widely used method to evaluate characteristics of materials where the increasing availability of experimental X-ray sources of high brilliance boosts its use^{1–3}. There are different regions within an XAS spectrum that are conveniently viewed by different interpretations. The region at the onset of absorption, i.e. from the edge up to a few eV, represents the near-edge X-ray fine structure (NEXAFS) or X-ray absorption near-edge structure (XANES). This part of the spectrum, as mainly addressed in our work, is sensitive to local chemistry as it probes low-lying conduction-band states in solids or low-lying empty orbitals in molecules.

Higher-energy transitions are known as the extended X-ray absorption fine structure (EXAFS), which is often interpreted in a scattering picture⁴, giving structural information through Fourier transforms. This renders EXAFS and XANES useful for structure determination even when lifetime broadening forbids observation of detailed near-edge structures².

In contrast to X-ray photoelectron spectroscopy (XPS) that is very surface sensitive due to the short path length of the escaping photoelectron (few⁵ nm), XAS has a penetration depth of several tens⁶ of nm.

Interestingly, electron energy-loss spectroscopy (EELS) signals are very similar to XAS for small momentum transfers typical for on-axis detectors with a small acceptance angle^{7,8}. Whereas recording high-resolution XAS spectra usually requires synchrotron radiation, EEL spectra can be conveniently measured in scanning transmission electron microscopes (STEMs), giving rise to the idea of a synchrotron in a microscope^{7,9}. Especially with modern electron monochromators¹⁰, STEM-EELS has become an increasingly powerful materials characterization tool, with a spatial resolution down to single atoms¹¹.

While in the photoelectron peaks in XPS are assigned to the core states they originate from, XAS (and EELS) data

is traditionally labeled as K -, L -, and M -edges, corresponding to core orbitals with respective principal quantum numbers $n = 1, 2, 3$. These edges represent sudden increases in the energy-dependent absorption cross-section corresponding to a resonance due to the respective core-state^{4,12}.

NEXAFS as well as the EELS near-edge fine structure can be interpreted within the single-particle picture as the excitation of a core electron to an empty state. As there are many empty states available, the NEXAFS spectrum originating from a single core orbital usually consists of several peaks, such that theoretical and computational support is indispensable for interpretation¹³.

There are several possible approaches for the simulation of XAS spectra as summarized in comprehensive reviews from different viewpoints^{4,14–17}. The most accurate calculations are based on equation of motion-coupled cluster theory (EOM-CCSD), providing reliable spectra both in terms of shape^{18,19} as well as excitation energies^{20,21}. However, such approaches are only applicable to smaller molecules due to their extreme computational cost.

The workhorse for describing excitations in larger systems is density functional theory (DFT). Here, the involvement of (highly) excited states suggests the use of time-dependent DFT (TDDFT)^{22,23}. However, TDDFT is also computationally expensive, and it has limitations in particular for the description of solids. An alternative to TDDFT are single-particle core-hole methods^{17,24,25} where the unoccupied states in the field of a core hole are interpreted as excitations. These methods are usually applied to K -edge spectra^{13,17,25–27} due to the difficulties of dealing with the angular momentum of the initial state and with spin-orbit (SO) coupling¹⁷, although several L -edge EELS simulations using the single-particle density of states²⁸ have notably been reported^{11,29–31}.

In solid systems, excited states that go beyond the single-particle picture can be described via configuration interaction methods³² or by solving the Bethe-Salpeter equation^{33,34}.

In this article, we apply single-particle methods to simulate L - and M -edge NEXAFS spectra, specifically focusing on $2p$ and $3d$ transitions. We compare our approach to experiment for molecules as well as for solids in order to explore their strengths and weaknesses, and also compare to TDDFT spectra in the case of molecules. The manuscript first discusses the picture underlying the description of NEXAFS spectra with an emphasis on comparing the transition from the many-particle to the single-particle viewpoint. A simple treatment of SO coupling is also presented. Then the predictions of the methods are compared to experiment both for molecules as well as for solid systems. After showing that our methodology works extremely well also for single-atom EEL spectra, we finish with conclusions.

II. X-RAY ABSORPTION

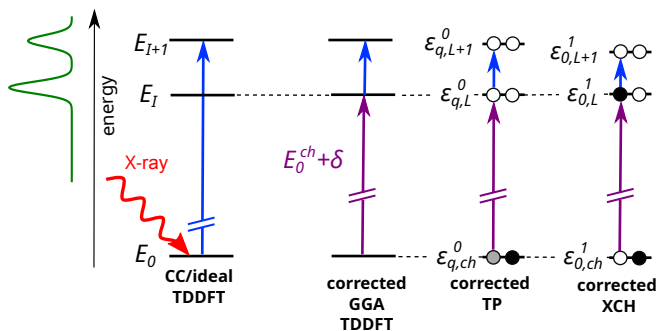


FIG. 1: Coupled cluster (CC)/ideal TDDFT energetics compared to strategies to obtain X-ray absorption spectra applied in this work. Many-particle energies are denoted as E_0 for the electronic ground states and $E_{I,I+1}$ for the first and second core-excited state, respectively. E_0^{ch} is the energy of the electronic "ground state" in presence of a core-hole.

Single particle energies as denoted as $\epsilon_{q,i}^Q$, where Q is the occupation of the lowest unoccupied molecular orbital ($i = L$) and q the occupation of the core state ($i = ch$). The alignment of the first peak energy to the corrected Δ -Kohn Sham energy (see text) $E_0^{ch} + \delta$ is indicated by the horizontal dashed lines.

The process of X-ray absorption can be interpreted in different approximations, as depicted schematically in Fig. 1. Generally, an X-ray photon is completely absorbed by the molecule or solid under observation, leading to a highly excited state of the system due to the large photon energy. The absorption cross-sections are proportional to the unitless oscillator strength^{24,35–37}

$$(f_I)_\eta = \frac{2m_e}{\hbar^2 e^2} (E_I - E_0) |\langle \Psi_I | \hat{\mathbf{u}}_\eta \cdot \mathbf{D} | \Psi_0 \rangle|^2, \quad (1)$$

where m_e is the electron mass, e the unit charge, \hbar the reduced Planck constant and $\eta = x, y, z$ are Cartesian coordinates. E_0 is the energy of the ground state, E_I the energy of the core-excited state of index I (there are many excited states

forming the full XAS-spectrum) and Ψ_0, Ψ_I denote their corresponding many-particle wave functions. The dipole operator in length form \mathbf{D} contains the contributions of all electrons. The relevant coordinate η is chosen by the polarization of the X-ray photon $\hat{\mathbf{u}}_\eta$. A specific $\hat{\mathbf{u}}$ appears in angle-dependent X-ray spectroscopy³⁸ or X-ray circular dichroism¹⁶. The target molecules or solids are usually in random orientations, such that the averaged intensity, i.e. $f_I = [(f_I)_x + (f_I)_y + (f_I)_z]/3$ is measured.

The calculation of transition energies and oscillator strengths in Eq. (1) can be performed in various approximations, where the most exact but also most demanding is the use of many-body wave functions as provided by coupled cluster (CC) descriptions for ground and excited states. The equivalent could be achieved by TDDFT in case the exact (frequency dependent³⁹) exchange-correlation kernel would be known. Practical TDDFT calculations, in particular based on gradient-corrected kernels as applied here, do not, however, necessarily lead to accurate transition energies⁴⁰.

XAS is often interpreted within the single-particle picture as transitions of a core electron to an empty orbital (or the conduction band for solids). The oscillator strength reduces in this picture to⁴¹

$$(f_{fc})_\eta = \frac{2m_e}{\hbar^2 e^2} \epsilon_{fc} |\langle \phi_f | \hat{\mathbf{u}}_\eta \cdot \mathbf{D} | \phi_c \rangle|^2, \quad (2)$$

where the matrix element is calculated from single-particle orbitals of the core state ϕ_c and the final state ϕ_f , and the dipole operator simplifies to $\mathbf{D} = -e\mathbf{r}$ with the electron spatial coordinate \mathbf{r} . The transition energies are now Kohn-Sham energy differences

$$\epsilon_{fc} = \epsilon_{q,i}^Q - \epsilon_{q,ch}^Q. \quad (3)$$

These single-particle energies may be again evaluated in different approximations that mainly differ by the occupation of the core state q as well as by the occupation Q of the lowest unoccupied state (LUMO). These choices not only influence the energy values, but also change the single-particle states in Eq. (2), where we have suppressed the labels q, Q for clarity. More details about the implementation can be found in the Supplementary Information (SI) Sec. II.

Regardless of whether single-particle or many-particle pictures are adopted, the calculated spectra are usually rigidly shifted to match their lowest energy peak with that of the experiment⁴². With the exception of computationally expensive EOM-CCSD calculations²² these shifts often amount to several eV.

Similar shifts appear in gas-phase XPS, where some of us have developed a semi-empirical method to obtain these from experimental data⁴³. In this method, we calculate the energy of the lowest energy transition as the energy difference between two DFT ground state calculations. One is the ground state energy E_0 and the other is the energy of the electronic ground state in the presence of the core-hole E_{ch}^0 . The zero indicates the overall electrical neutrality of this configuration, i.e. it contains an extra valence electron as relevant for XAS.

Despite the principal difficulty of describing such a high-energy core-excited state within DFT ground-state theory to obtain E_{ch}^0 , the similarity to the equivalent-core approximation¹⁶ rationalizes this approach. The first transition energy, known as Δ -Kohn Sham energy (Δ KS), is then

$$E_B^0 = E_{ch}^0 - E_0. \quad (4)$$

Local and semilocal functionals are rather accurate in the evaluation of ionization potentials and electron affinities from total energy differences⁴⁴, even better than computationally much more demanding GW approximations⁴⁵. Nevertheless, the core-hole energies calculated from Eq. (4) are observed to be shifted against the experiment, where the shift depends on the core state and the functional, but not on the chemical environment^{13,43}. This makes it possible to obtain a semi-empirical correction by comparing a large body of calculations with experimental data E_B^{exp} to obtain shift values

$$\delta = E_B^{\text{calc}} - E_B^{\text{exp}} \quad (5)$$

that can be used to correct the raw calculated energies E_B^{calc} as indicated in Fig. 1. This method has successfully predicted the XPS spectra of ionic clusters⁴⁶ and carbon materials^{47,48}, as well as to S 1s NEXAFS spectra^{3,13}. We will see below that there is also substantial uncertainty in experimental absolute energies. The shift δ can therefore be seen as an average over experimental knowledge. There are hints that at least a large part of the shift stems from the use of the frozen-core approximation, as all-electron calculations seem to have negligible shifts at least for light elements^{49,50}.

In contrast to K edges (s -type core states), L and M edges have finite orbital angular momenta and are thus subject to spin-orbit (SO) coupling⁵¹. The SO coupling arises from the relativistic Dirac equation and couples the spin quantum s to the orbital angular momentum l , leading to two different core-state energies for the same orbital. This SO splitting is larger for orbitals of high binding energy, while it has comparably small effects on the valence or empty (conduction band) states. The SO splitting usually also depends negligibly on the chemical environment¹⁹ and δ from Eq. (5) applies to both SO split energies. This is equivalent to defining one shift δ for each SO split state, where the two δ are separated by the SO splitting. The contributions of the two states are then approximated as the same spectrum separated in energy by the SO splitting and weighted according to the relative spin multiplicities^{46,52}.

Having obtained an accurate value for the first transition energy, i.e. to the LUMO in NEXAFS spectra, the question appears how to describe higher-lying states (c.f. Fig. 1). The natural choice in the framework of DFT seems to be TDDFT, as often applied in the literature but with mixed success. TDDFT is based on ground-state orbitals, where it can only describe single excitations if the usual energy-independent kernels are used³⁹. The orbitals in the field of the core-hole may be better suited to describe the final state after photon absorption¹⁶. These orbitals already represent multiple excitations with respect to the ground-state orbitals. Along these

lines, the maximum-overlap method⁵³ that considers the orbital changes under excitation is very successful, and sometimes even exceeds TDDFT accuracy in practical calculations.

K -edge NEXAFS spectra have therefore been successfully calculated within a single-particle picture, where the corresponding orbitals are obtained within the field of an explicit core-hole. There are different approximations possible¹⁷, and it has turned out that the transition-potential (TP) method^{25,26,54} with $Q = 0$ and $q = 1/2$ in Eq. (3) often leads to a rather good agreement with experiment^{13,41}. The excited core-hole (XCH) method, where $Q = 1$ and $q = 0$ in Eq. (3) as appropriate for a neutral excitation, was also successfully applied^{24,55}. The system's neutrality in XCH greatly benefits periodic calculations.

III. COMPUTATIONAL SETTINGS

The electronic structure of the molecules and solids considered is described by DFT within the projector augmented wave method⁵⁶ as implemented in GPAW⁵⁷⁻⁵⁹. The exchange-correlation energy was evaluated as devised by Perdew, Burke and Ernzerhof⁶⁰.

Molecules were simulated in Dirichlet (non-periodic) boundary conditions, where the simulation cell contained at least 5 Å around each atom. Solids and the two-dimensional (2D) structures are calculated in periodic boundary conditions. The 2D systems included at least 10 Å of distance between the layers to avoid their interaction. All structures were relaxed until all forces were below 0.05 eV/Å.

The smooth part of the Kohn-Sham orbitals as well as of the electron density are represented on real-space grids for most of the calculations. The grid spacing of the Kohn-Sham orbitals is 0.2 Å, while it is 0.1 Å for the electron density. The Kohn-Sham orbitals in the 2D system were represented by plane waves with an energy cut-off of 600 eV.

We use the frozen-core approximation for orbitals not participating to the valence band, which are calculated for free atoms. The frozen-core approximation allows to describe the presence of a core hole obtained by a self-consistent free-atom calculation with a reduced occupation q of the core state²⁶. This approach explicitly considers a localized core hole and thus avoids problems with delocalized core-hole states in symmetric environments¹⁷. Details about the calculation of the shifts δ [Eq. (5)] are found in SI Sec. III.

We contrast these single-particle calculations with linear-response TDDFT (LrTDDFT) calculations³⁵, where we include the relevant core-states into the valence orbitals. There is thus no explicit core-hole present in our LrTDDFT that is purely based on Kohn-Sham ground-state orbitals.

The SO splittings are calculated through perturbation theory^{59,61} for free atoms. We have checked that the calculated SO-splittings vary very little compared to their values within the molecules, such that the assumption of a common SO splitting per element and core-state is a good approximation independent of the chemical environment (see SI Sec. IV for details).

The oscillator strengths from Eq. (1) calculated via LrT-DDFT or from Eq. (2) calculated via DFT use the corrected energies involving the shifts δ . In order to compare the spectra to experiment, these oscillator strengths are folded (convolved) by Cauchy distributions (Lorentzians) of variable width modeling to finite lifetime, vibrational contributions⁶² and limited experimental resolution. The EEL spectra cover a larger range of excitation energies than the XAS spectra and higher-energy excitations are expected to have shorter lifetimes, resulting in larger broadening. This is taken into account by energy dependent broadening as detailed in SI. The convolution procedure generally results in intensities that are folded oscillator strengths (FOS) with the unit $1/\text{eV}$.

IV. RESULTS AND DISCUSSION

A. Molecules

In this section we compare calculated spectra in different approximations to experiment. We in particular emphasize the comparison of the many-particle spectra determined by LrTDDFT to fixed core-hole single-particle approximations in the XCH (full core hole $q = 0$ and extra electron in LUMO $Q = 1$) and the TP (half core-hole $q = 1/2$ and $Q = 0$) approximations.

The Ti $L_{3,2}$ edge spectra of TiCl_4 are presented in Fig. 2. There are two experimental spectra for this molecule available in the literature^{63,64}, which are similar in the appearance of two main peaks, but there are significant differences also. The spectra differ in peak-width (different experimental conditions), absolute peak positions (difficulties in determining the absolute energy scale), and in the relative energy separation of the peaks.

We generally evaluate the agreement between two spectra by calculating the coefficient of determination R^2 value^{65–67}, where a value of unity describes perfect agreement. We allow for a variable width of the Cauchy distributions as well as for a variation in absolute energy by a shift ω to optimize agreement with experiment (see SI Sec. VI for details). Note that the shift ω is for a specific experiment, while the shift δ from Eq. (5) corrects the calculation to the average of high energy resolution experiments. We therefore regard our calculated and corrected energy as an accurate energy scale to which the specific experiment will be corrected.

We first compare the two experimental spectra for TiCl_4 in a similar way with each other. Here the more resolved spectrum of Stener et al.⁶⁴ has to be shifted by $\omega = -1.4$ eV to maximize R^2 , still leading to a low $R^2 = 0.47$. The energetic distance between the main peaks caused by spin-orbit splitting is 5 and 5.5 eV in the two experiments respectively, and therefore also different (our calculated SO splitting value is 5.85 eV for Ti $2p$). These disagreements show the experimental difficulties in the precise determination of energy scales.

The better resolved spectrum of Stener et al.⁶⁴ shows a very small peak, about 2 eV lower than the main feature and well separated $2p^{1/2}$ contributions above 464 eV. These features are well described by the LrTDDFT calculations resulting in a

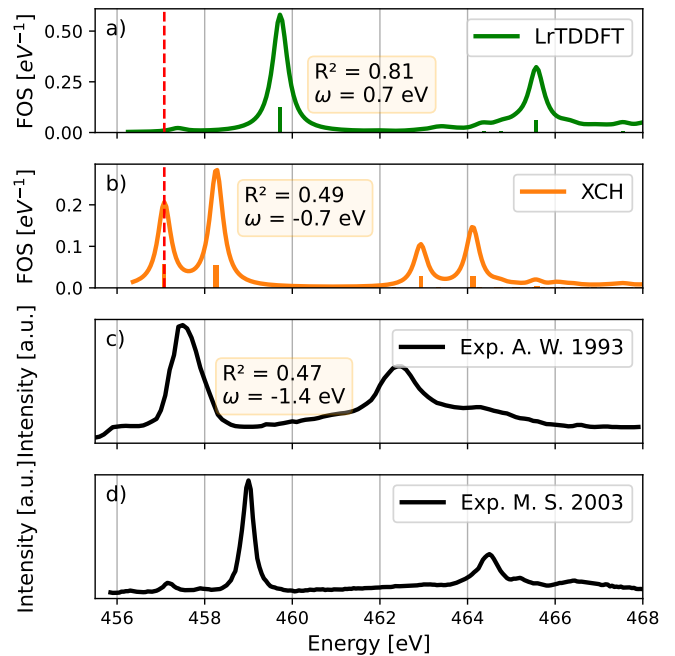


FIG. 2: Ti $2p$ or $L_{2,3}$ -edge NEXAFS spectra for TiCl_4 . The experimental spectrum in c) is adapted from Ref. 63 and that in d) from Ref. 64. The oscillator strength of each transition is shown as a stick spectrum. The energetic position of the first excitation that is aligned to the corrected ΔKS is marked by the dashed vertical red line. The folded oscillator strength (FOS) is obtained by from the stick spectrum as explained in the text. The optimal R^2 and the corresponding energy shift ω applied to the experiment in d) is given (the experimental spectra are still depicted on their original energy scale, but were shifted to evaluate R^2).

rather large R^2 . Similar agreement has been found from related calculations⁶⁴. The energy of the first transition that is shifted to the corrected ΔKS energy is indicated in the figure. This energy notably corresponds to a transition with very small oscillator strength, which therefore does not appear in the spectrum.

The single-particle XCH spectrum looks very different, however, and also shows a low R^2 . There are two strong peaks in the low-energy region caused by the $2p_{3/2}$ contribution. These correspond to the unoccupied Ti $3d$ shell that is split due to the symmetry of the four Cl atoms. The corresponding $2p$ to $3d$ transitions are obviously coupled by LrTDDFT, but this is not the case within the single-particle picture. This coupling of empty states is known from atomic physics and is dubbed the multiplet effect in the literature⁶⁹.

The spectrum of the sulfur $L_{2,3}$ edge or S $2p$ for the SO_2 molecule is depicted in Fig. 3. The experimental spectrum⁶⁸ shows two shallow peaks on the lower energy side at 164.5 and 166 eV and several peaks with larger intensity starting from 169 eV. The transitions above 171 eV show a clear peak structure that is assigned to Rydberg states⁶⁸. As we model the vibrational broadening by a fixed folding width, our sim-

ulation cannot describe this highly resolved region. Vibrationally resolved simulations have been demonstrated^{62,71,72}, but go well beyond our approach here.

All simulated spectra qualitatively describe this general structure of the spectrum, and the positions of the peaks are in overall agreement. The linear-response TDDFT spectrum is slightly more blurred for the strong transitions than the single-particle approaches. Similarly to their visual appearance, all methods have a good accuracy, but the single-particle approaches are clearly superior to LrTDDFT in terms of the R^2 value.

The calculated $L_{2,3}$ edge spectra of thiophene (C_4H_4S) are compared to the experiment in Fig. 4. Similar to SO_2 , we observe a generally good agreement when using core-hole methods, but the LrTDDFT spectrum is very blurred, such that no peak structure is visible anymore. This is reflected in its lower value R^2 compared to TP and XCH. The experimental spectrum has to be shifted by 0.3–0.8 eV to maximize R^2 , i.e., slightly more than in the case of SO_2 .

Next, we turn to the $L_{2,3}$ edge of silicon, where we first address the spectrum of SiH_4 in Fig. 5. The experimental spectrum can be separated into two regions, where the transitions below 104.5 eV are largely broadened. The transitions above this energy show a clear peak structure that is assigned to the vibrational sidebands of the Rydberg states⁷³. Similarly to the higher-energy peaks in SO_2 , the assumption of a fixed folding hinders the description of these narrow transitions.

The calculations agree rather well to experiment in the first

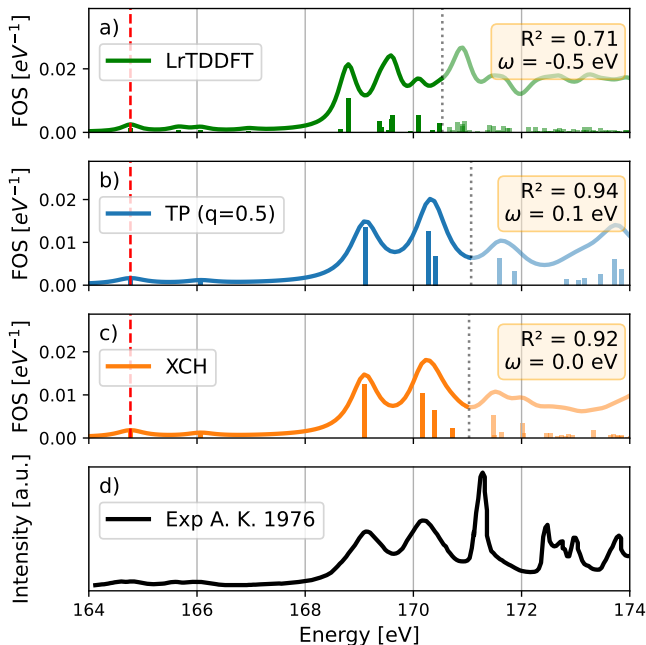


FIG. 3: Calculated $S\ 2p$ or $L_{2,3}$ -edge NEXAFS spectra for SO_2 and d) an experimental spectrum adapted from Ref. 68.

The spectral region used for obtaining the R^2 value is depicted in solid color separated from the spectral region excluded by the black dotted line (see text for details).

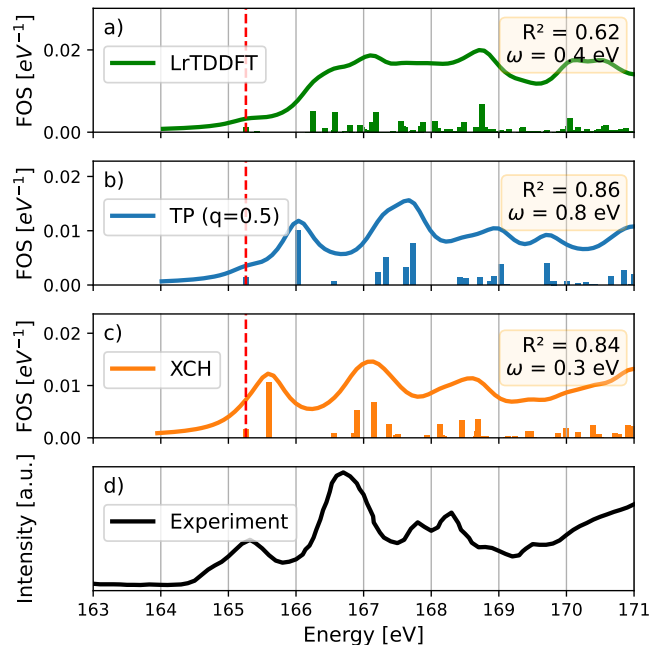


FIG. 4: As Fig. 3, but for thiophene. The experimental spectrum is adapted from Ref. 70.

broad peak and also describe the less intense (after averaging in the experiment) higher-energy region. Taking only the

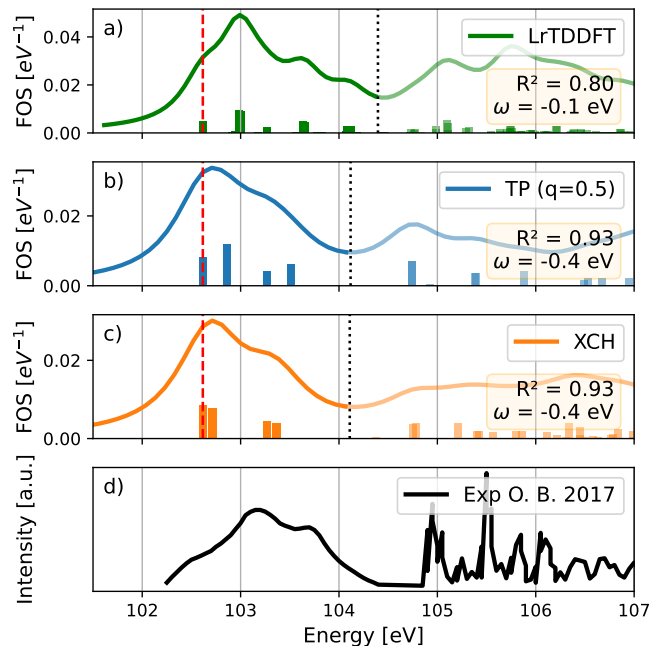


FIG. 5: $Si\ 2p$ or $L_{2,3}$ -edge NEXAFS spectra for SiH_4 . The experimental spectrum is adapted from Ref. 73. The spectral region used for obtaining the R^2 value and the corresponding shift ω is depicted in solid colour (see text for details).

lower-energy peak into account leads to rather large R^2 values, where the single-particle approaches outperform LrTDDFT. Only small shifts must be applied to the experimental spectrum to maximize R^2 .

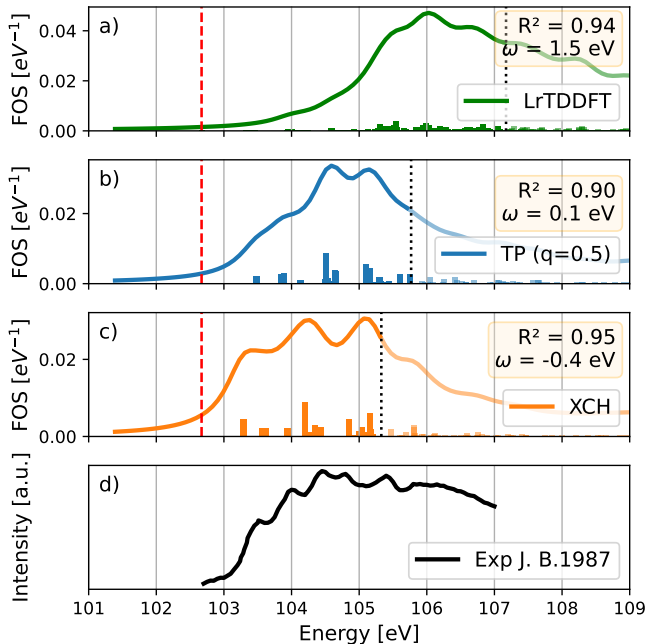


FIG. 6: Si $2p$ or $L_{2,3}$ -edge NEXAFS spectra for $\text{Si}(\text{CH}_3)_4$. The experimental spectrum is adapted from Ref. 74.

The $L_{2,3}$ edge spectra of $\text{Si}(\text{CH}_3)_4$ are compared in Fig. 6. The experimental spectrum mainly consists of a broad peak with some visible substructure. This is reflected in all simulations, but the shifts of this broad peak relative to the first transition at ΔKS are quite different. LrTDDFT shows the largest shift of this broad peak to higher energies. This is reflected in the largest shift ω needed to maximize the agreement of LrTDDFT compared to TP and XCH. The flexibility of these different shifts results in similar R^2 values for all models.

The Si $L_{2,3}$ edge spectra of SiCl_4 are shown in Fig. 7. Here, the experimental spectrum is very structured, with clearly observable peaks in the range from 104 to 111 eV. There are two regions with relatively high intensity separated by a region of lower intensity within this energy range. All simulations represent this general shape of the experimental data, where the low-intensity region is the smallest in the LrTDDFT spectrum. The R^2 values are relatively small due to the mismatch of the peak intensities, where the simulations give a larger weight to the higher-energy peaks compared to experiment. The shift ω that must be applied to the experimental spectrum to maximize R^2 is very similar between -0.7 and -0.8 eV for all calculations.

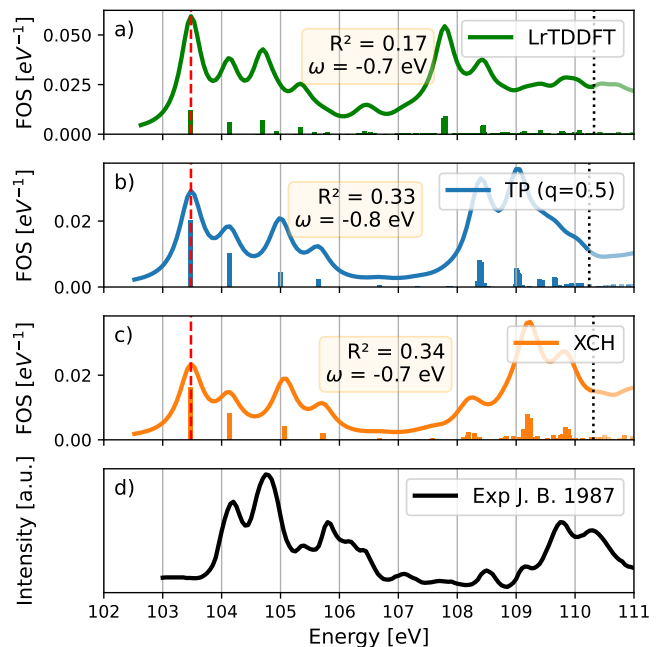


FIG. 7: Si $2p$ or $L_{2,3}$ -edge NEXAFS spectra for SiCl_4 . The experimental spectrum is adapted from Ref. 74.

B. Solids

We then consider solids, which we describe in a bulk approximation without the consideration of a surface. We first examine the Ti $L_{2,3}$ edge or the Ti $2p$ core-transitions. We analyze three different solid systems that feature a Ti $2p$ core hole in the following: SrTiO_3 , the rutile structure of TiO_2 , and the anatase structure of TiO_2 .

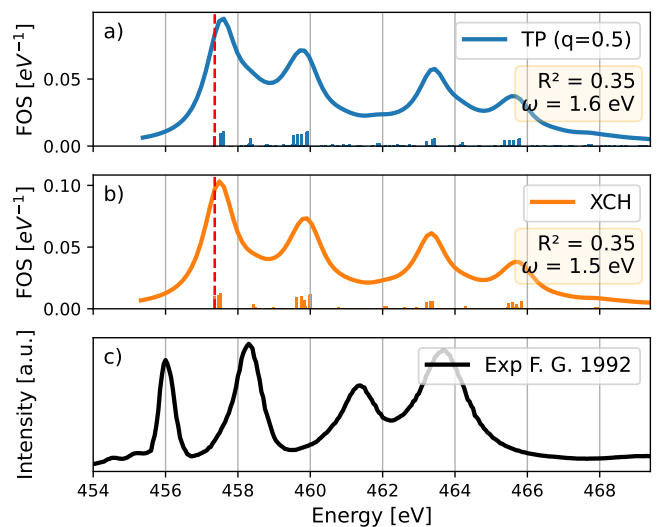


FIG. 8: Ti $2p$ or the $L_{2,3}$ -edge NEXAFS spectra for solid SrTiO_3 . The experimental spectrum is adapted from Ref. 75.

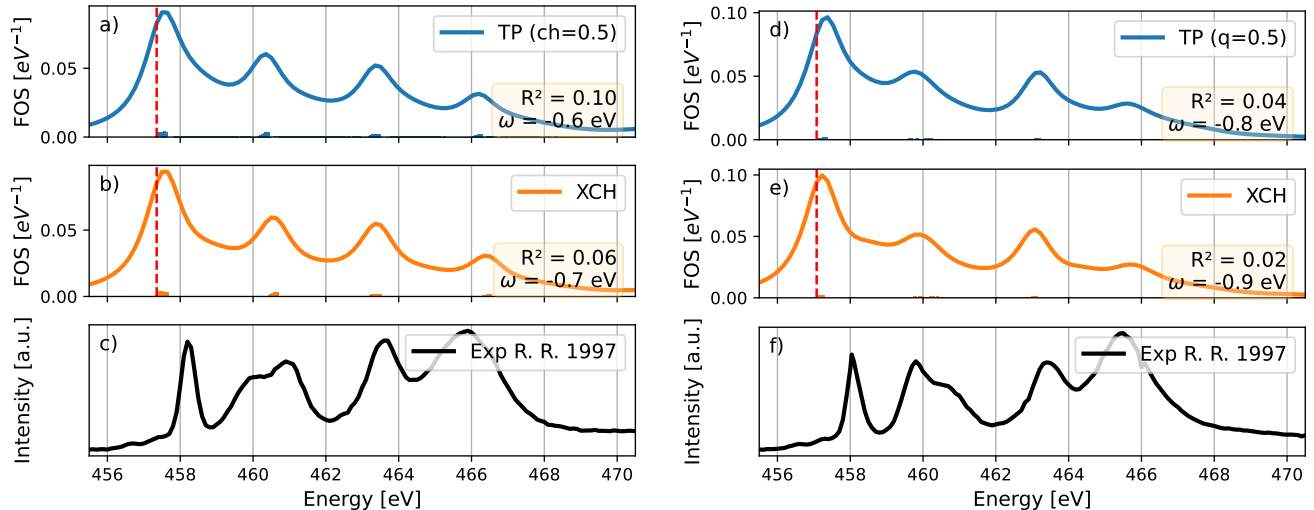


FIG. 9: Ti $2p$ or the $L_{2,3}$ -edge NEXAFS spectra for solid TiO_2 a-c) rutile and d-f) anatase structure. The experimental spectra are adapted from Ref. 76.

The unit cell of SrTiO_3 has a $Pm\bar{3}m$ structure. The initial structure was obtained from the Materials Project (MP)⁷⁷ with ID: mp-5229 and subsequently re-relaxed in a $[3 \times 3 \times 3]$ supercell. The Brillouin zone was sampled using three k -points in each direction. The Ti $2p$ XAS spectrum of SrTiO_3 , has been investigated experimentally⁷⁵ and theoretically^{34,78–80} in great detail in the literature. The spectra are presented in Fig. 8, where the experimental spectrum⁷⁵ consists of four main peaks with varying widths. Both TP and XCH qualitatively reproduce this general peak structure.

A more detailed investigation of the first peak unveils the similarity of this peak with the Ti $3d$ contributions in the spectrum of TiCl_4 in Fig. 2. The multiplet effect not covered by the single-particle approaches is present also in SrTiO_3 . While the explicit core-hole methods XCH and TP are able to describe the overall structure of the four peaks successfully, the multiplet effect needs many-body approaches such as configuration interaction³² or solutions of the Bethe-Salpeter equation³⁴. We note, however, that a 20.4 eV shift had to be applied there to align the theoretical and experimental first peaks.

We next turn to TiO_2 with its most common rutile and anatase crystal structures. The TiO_2 rutile structure belongs to the Pm_4/mnm space group, where the initial structure from MP with ID mp-2657 was re-relaxed in the $2 \times 2 \times 3$ supercell. The Brillouin zone was sampled by five k -points in each direction. The TiO_2 anatase structure is part of the $I4_1/amd$ space group, where the initial structure from MP with ID mp-390 was re-relaxed in the $3 \times 3 \times 1$ supercell. The Brillouin zone was also sampled by five k -points in each direction. The calculated spectra for rutile are shown in Fig. 9 a) and b), while c) displays an experimental spectrum reported in Ref. 76. In Fig. 9 d), e), and f), we present similar data for the anatase structure, using the experimental spectra from the same study.

The R^2 values for these spectra are notably low, between 0.02 – 0.10. However, we note that the four peaks are present in approximately the expected region. The theoretical spectra

also indicate a shift towards lower energies. Since the core-hole methods successfully reproduce the four peaks, it can be argued that they somewhat replicate the spectra. Yet, we face similar issues as with SrTiO_3 , as we did not account for many-body effects and charge-transfer multiplet effects. Additionally, the theoretical spectra for the two structures appear quite similar. It is widely recognized that the best way to differentiate between rutile and anatase structures in XAS spectra is to analyze the peaks in the 459–462 eV range; this is where their only differentiation lies. Anatase features a more pronounced first peak, whereas rutile displays a stronger second peak⁷⁶. This distinction is somewhat observable in that range, yet we cannot definitively separate these TiO_2 structures using core-hole methods.

We now consider NiO, an antiferromagnetic solid that exhibits a rocksalt crystal structure with a lattice constant of $a = 4.19\text{\AA}$ ^{77,83}. We use a $2 \times 2 \times 2$ cubic supercell and sample the Brillouin zone with five k -points in each direction.

The spectra are displayed in Fig. 10, where we display two spectra from the literature^{81,82} that encompass different energy ranges. The two experimental spectra align rather well, as indicated by the high R^2 value and the minor shift of $\omega = -0.8$ eV required to align the energy scales. Both experiments show a prominent peak around 853 eV that is accompanied by at least one smaller peak at slightly higher energy. The Ni $2p_{1/2}$ contribution is visible above 870 eV.

When comparing the two theoretical spectra to the experimental spectra in d), we notice that they are both in quite good agreement. They reproduce the general shape of the spectra; however, the proportions in the XCH in b) seem exaggerated, while the TP method offers a more accurate representation. This is also reflected in the R^2 values. The comparison between the theoretical spectra and the experimental results in c) can be found in Sec. VI in SI.

However, Ikeno et al. also investigated the NiO spectra, as Ni is a transition metal, and found that by incorporating the CI

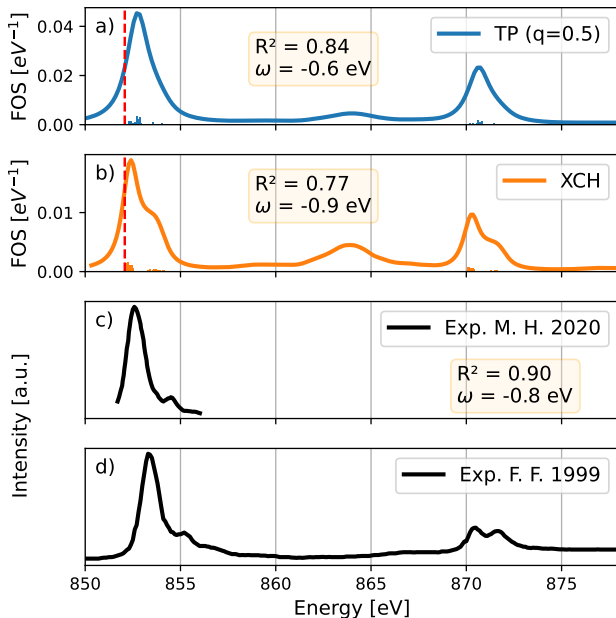


FIG. 10: Ni $2p$ or the $L_{2,3}$ -edge NEXAFS spectra of solid NiO. The experimental spectrum in c) is adapted from Ref. 81, and the experimental spectrum in d) is adapted from Ref. 82.

method and multiplet effects, a better agreement with the experiments was achieved³². Although these methods produce improved spectra, the agreement derived from the TP is adequate to characterize the NiO structure; we believe this is due to the fact that, unlike the Ti structures, the NiO d -bands are partly filled, whereas the d -bands for the Ti structures are entirely open.

We also wish to address the $M_{4,5}$ NEXAFS spectra, specifically concerning d -type core holes. Here, we have selected tin as element and compared our calculations to the available experimental spectrum of stannic oxide (SnO_2). There are numerous gas-phase XPS spectra for Sn $3d$, making the fit for the corresponding absolute shift δ unproblematic, as shown in Fig. S3 in SI. Unfortunately, we have not found any molecular NEXAFS spectrum for comparison. Thus, we are limited to the bulk phase, excluding TDDFT.

SnO_2 exhibits a rutile crystal structure⁸⁵ (space group $P4_2/mnm$) with lattice constants $a = b = 4.76 \text{ \AA}$, $c = 3.21 \text{ \AA}$.⁷⁷ The initial structure was sourced from the Materials Projects SnO_2 , with the materials ID: mp-856.⁷⁷ Our calculation is done with a $2 \times 2 \times 3$ supercell with six k -points in each direction; however, the calculations converge with four k -points. Further details can be found in Secs. VII and VI in SI.

Fig. 11 shows the spectra produced by the TP method with $q = 0.5$ in a), TP with $q = 0.33$ in b), and the XCH method in c). The experimental spectra by Chuvenkova et al.⁸⁴ is shown in d). All theoretical spectra consistently reproduce the features of the experiment in d) with quite high R^2 values, with the TP ($q = 0.33$) and XCH methods demonstrating the best agreement. However, the XCH spectrum shows the smallest

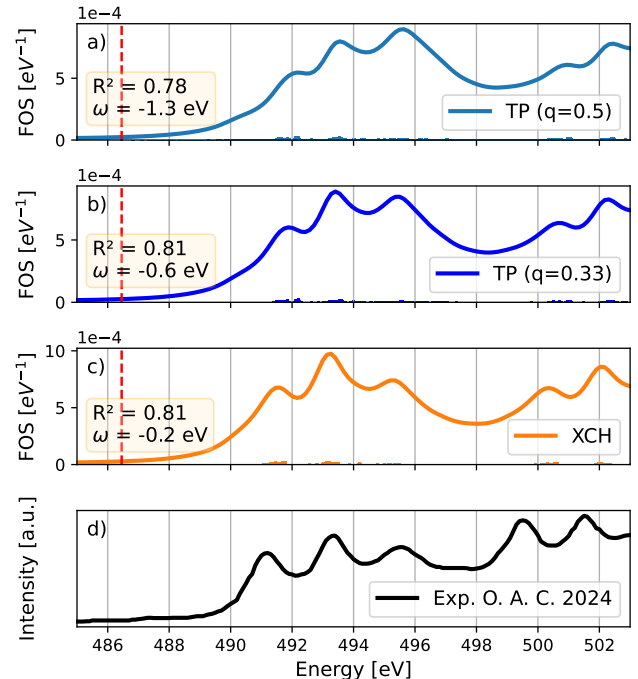


FIG. 11: Sn $3d$ or the $M_{3,4}$ -edge NEXAFS spectra of SnO_2 . The experimental spectrum is adapted from Ref. 84.

energy shift compared to the experiment.

C. Electron energy-loss in graphene

We finally address the comparison of our calculations nominally meant for simulating XAS spectra to experimental electron energy-loss spectra of single silicon atoms embedded in graphene defects. Ramasse et al. have shown that these spectra can be used to distinguish three- from four-bonded silicon atoms at defects³⁰.

The structures are modeled by a 4×4 single-layer graphene sheet with lattice constant of $a = 2.46 \text{ \AA}$ ⁸⁶. A single Si atom substitutes a single C atom in the three-bonded configuration, while a single Si atom substitutes two C's in the four-bonded configuration. The Si atoms were displaced out of the plane and the structure was allowed to relax. This led to a back-relaxation into the plane for the four-bonded Si, while the three-bonded Si stayed out of the plane due to its larger size compared to the replaced C atom. The relaxed structures are shown in Fig. 12 a) and e), respectively. The calculations are done in periodic boundary conditions. The Brillouin zone is sampled by seven k -points in x and y directions while only using the Gamma point in z direction.

Fig. 12 shows the spectra produced by the XCH method, the TP method with $q = 0.5$ and the TP with $q = 0.9$, for both the four- and three-bonded Si defect, in b-d) and f-h) respectively. The agreement of the calculations with the experiment is of such quality, that the spectra can be directly overlaid, as reflected also by the large values of R^2 .

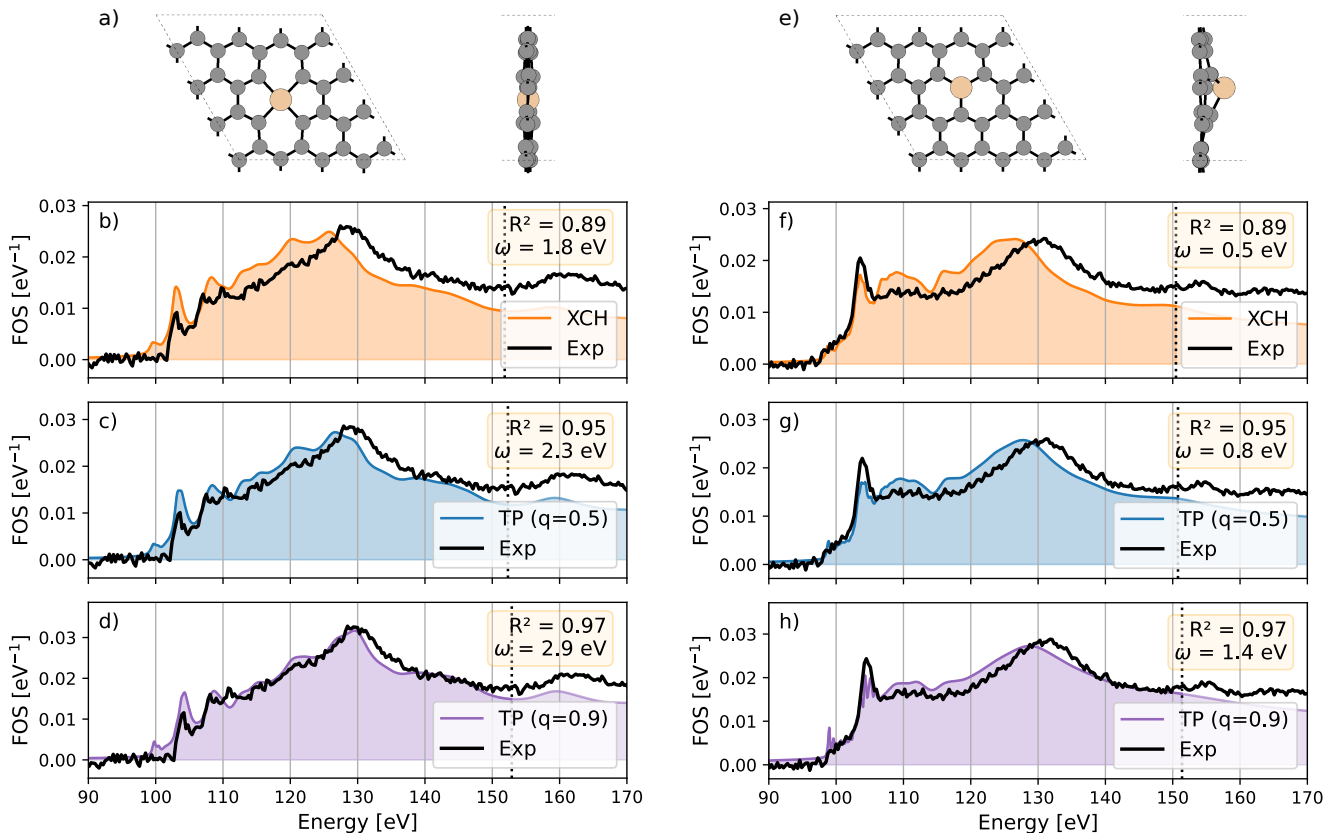


FIG. 12: (a and e) Structural model of a single Si atom covalently bound into a vacancy in single-layer graphene as a (a) four-bonded and (e) three-bonded substitution. (b-d and f-h) Calculated Si $2p$ or $L_{2,3}$ -edge XAS spectra for a single Si atom in a graphene defect, represented in a) and e), compared to a single-atom EELS measurement. The TP methods consider two core-hole occupancies of $q = 0.5, 0.9$. The experimental spectra are from Ref. 30. The experimental spectra are shifted by ω given in the caption to maximize R^2 in each case.

Alignment of the first prominent peaks around 105 eV leads to a small mismatch of the broad peaks around 130 eV, where in particular the XCH is at slightly lower energy. This suggests insufficient screening of the full core-hole in XCH, compared to TP with $q = 0.5$. Indeed, the reduction of the core-hole to $q = 0.9$ helps in this respect, leading to very good agreement for both binding situations. The predicted spectra indeed allow to distinguish the binding mode, as is explicitly shown in Fig. S7 in SI. Overall, it is remarkable how well the simulations are able to reproduce the EELS fine structure, as has also been observed previously without consideration of an explicit core-hole^{11,29–31}.

V. CONCLUSIONS

In conclusion, we have demonstrated a straightforward method to simulate X-ray absorption spectra for core-states with finite orbital angular momentum. The method is based on single-particle orbitals in the field of a core-hole and does not require the explicit consideration of spin-orbit splitting. We have compared the two mainly used approaches in the liter-

ature, excited core-hole (XCH) and transition-potential (TP), that differ in the occupation of the core-hole state as well as the overall charge in the calculation.

Both the XCH and TP methods accurately replicate the $L_{2,3}$ -edge XANES experimental spectra for the majority of the molecular systems examined. Their performance is comparable to the LrTDDFT method and, in some instances, even surpasses it. In our comparison of the TP and XCH methods for molecular systems, we observed similar R^2 values, with the XCH method being slightly higher in Si cases and the TP method in S cases. For solid systems, TP slightly outperformed XCH in most instances, except for SnO_2 , where XCH achieved better results. The comparison with experimental EEL spectra is improved when the occupation of the core-hole is further reduced than in the traditional TP using a half occupied core-hole, however.

LrTDDFT showed a clear advantage over the single-particle methods with the Ti L -edge for TiCl_4 , where the Ti has a fully open d -band due to the multiplet effect. This mixing of unoccupied states due to many-body effects is present only in LrTDDFT and cannot be reproduced by single-particle methods.

A similar picture emerges for solid systems, where the core-hole methods also sufficiently reproduce the $L_{2,3}$ and $M_{4,5}$ edge XANES experimental spectra. Also, at least for graphene, single-atom electron energy-loss spectra can be simulated with excellent accuracy. However, we encountered similar challenges as with the molecular TiCl_4 due to missing multiplet effects that require a many-body description.

Overall, the explicit core-hole TP and XCH methods are able to sufficiently describe $L_{2,3}$ -edge XANES for the majority of systems we evaluated. There is no clear preference for either of the two methods as their advantages and disadvantages seem to be system-dependent. Nevertheless, the methods described represent a computationally cheap method to simulate XAS spectra with an overall good agreement to experiment on the absolute energy scale.

Our implementation has the advantage of being fully open source, and we can thus expect such simulations to become more widely accessible for the X-ray and electron microscopy communities.

ACKNOWLEDGMENTS

E. J. and M. W. thank L. Mayrhofer and M. Moseler for useful discussion and for reading the manuscript. E. J., N. H. and M. W. acknowledge funding by the Deutsche Forschungsgemeinschaft (DFG, German Research Foundation) via the Excellence Cluster LivMatS under Germany's Excellence Strategy—EXC-2193/1—390951807. E.J. and M.W. are thankful for the computing resources provided by the state of Baden-Württemberg through bwHPC and the German Research Foundation through grant number INST 40/575-1 FUGG (NEMO and JUSTUS2 clusters). We thank Quentin Ramasse for providing the raw data for the experimental EEL spectra considered in this study.

VI. AUTHOR DECLARATIONS

A. Conflict of Interest

The authors have no conflicts to disclose.

B. Author Contributions

Esther A. B. Johnsen: Theoretical analysis (equal); Calculations (lead); Writing – review & editing (equal); Naoki Horiuchi: Calculations (equal); Toma Susi: Writing – review & editing (equal); Michael Walter: Calculations (equal); Theoretical analysis (lead); Conceptualization (lead); Resources (lead); Supervision (lead); Writing – review & editing (equal).

DATA AVAILABILITY STATEMENT

Data is available on request from the authors. The code developed to perform these calculations will soon be available

in the GPAW library.

- ¹M. Müller, S. Choudhury, K. Gruber, V. B. Cruz, B. Fuchsichler, T. Jacob, S. Koller, M. Stamm, L. Ionov, and B. Beckhoff, "Sulfur x-ray absorption fine structure in porous li-s cathode films measured under argon atmospheric conditions," *Spectrochimica Acta Part B: Atomic Spectroscopy* **94-95**, 22–26 (2014).
- ²Z. Zeng, S. Küspert, S. E. Balaghi, H. E. M. Hussein, N. Ortlieb, M. Knäbbeler-Buß, P. Hügenell, S. Pollitt, N. Hug, J. Melke, and A. Fischer, "Ultrahigh mass activity pt entities consisting of pt single atoms, clusters, and nanoparticles for improved hydrogen evolution reaction," *Small* **19**, 2205885 (2023).
- ³R. Matsidik, K. Skudler, S. de Kock, A. Seifert, M. Müller, M. Walter, S. Choudhury, and M. Sommer, "On the effect of sulfur strand length on the electrochemical performance of dual-redox-active sulfur-naphthalene diimide cathode materials," *ACS Applied Energy Materials* **6**, 9466–9474 (2023).
- ⁴J. J. Rehr and R. C. Albers, "Theoretical approaches to x-ray absorption fine structure," *Reviews of Modern Physics* **72**, 621–654 (2000).
- ⁵F. A. Stevie and C. L. Donley, "Introduction to x-ray photoelectron spectroscopy," *Journal of Vacuum Science & Technology A* **38**, 063204 (2020).
- ⁶C. Peth, F. Barkusky, and K. Mann, "Near-edge x-ray absorption fine structure measurements using a laboratory-scale XUV source," *Journal of Physics D: Applied Physics* **41**, 105202 (2008).
- ⁷R. F. Egerton, "Electron energy-loss spectroscopy in the tem," *Reports on Progress in Physics* **72**, 016502 (2008).
- ⁸S. Löffler, I. Ennen, F. Tian, P. Schattschneider, and N. Jaouen, "Breakdown of the dipole approximation in core losses," *Ultramicroscopy* **111**, 1163–1167 (2011).
- ⁹L. M. Brown, "A synchrotron in a microscope," in *Electron Microscopy and Analysis 1997, Proceedings of the Institute of Physics Electron Microscopy and Analysis Group Conference, University of Cambridge, 2-5 September 1997* (CRC Press, 1997) 1st ed., p. 6.
- ¹⁰O. L. Krivanek, T. C. Lovejoy, N. Dellby, T. Aoki, R. W. Carpenter, P. Rez, E. Soignard, J. Zhu, P. E. Batson, M. J. Lagos, R. F. Egerton, and P. A. Crozier, "Vibrational spectroscopy in the electron microscope," *Nature* **514**, 209–212 (2014).
- ¹¹T. Susi, T. P. Hardcastle, H. Hofsäss, A. Mittelberger, T. J. Pennycook, C. Mangler, R. Drummond-Brydson, A. J. Scott, J. C. Meyer, and J. Kotakoski, "Single-atom spectroscopy of phosphorus dopants implanted into graphene," *2D Materials* **4**, 021013 (2017).
- ¹²F. M. F. de Groot, H. Elnaggar, F. Frati, R.-p. Wang, M. U. Delgado-Jaime, M. van Veenendaal, J. Fernandez-Rodriguez, M. W. Haverkort, R. J. Green, G. van der Laan, Y. Kvashnin, A. Hariki, H. Ikeno, H. Ramanantoanina, C. Daul, B. Delley, M. Odelius, M. Lundberg, O. Kuhn, S. I. Bokarev, E. Shirley, J. Vinson, K. Gilmore, M. Stener, G. Fronzoni, P. Declava, P. Kruger, M. Retegan, Y. Joly, C. Vorwerk, C. Draxl, J. Rehr, and A. Tanaka, "2p x-ray absorption spectroscopy of 3d transition metal systems," *Journal of Electron Spectroscopy and Related Phenomena* **249**, 147061 (2021).
- ¹³S. d. Kock, K. Skudler, R. Matsidik, M. Sommer, M. Müller, and M. Walter, "NEXAFS spectra of model sulfide chains: implications for sulfur networks obtained from inverse vulcanization," *Physical Chemistry Chemical Physics* **25**, 20395–20404 (2023).
- ¹⁴N. A. Besley, "Density functional theory based methods for the calculation of x-ray spectroscopy," *Accounts of Chemical Research* **53**, 1306–1315 (2020).
- ¹⁵N. A. Besley, "Modeling of the spectroscopy of core electrons with density functional theory," *WIREs Computational Molecular Science* **11**, e1527 (2021).
- ¹⁶P. Norman and A. Dreuw, "Simulating x-ray spectroscopies and calculating core-excited states of molecules," *Chemical Reviews* **118**, 7208–7248 (2018).
- ¹⁷B. P. Klein, S. J. Hall, and R. J. Maurer, "The nuts and bolts of core-hole constrained ab initio simulation for k-shell x-ray photoemission and absorption spectra," *Journal of Physics: Condensed Matter* **33**, 154005 (2021).
- ¹⁸M. Schreiber, M. R. Silva-Junior, S. P. A. Sauer, and W. Thiel, "Benchmarks for electronically excited states: CASPT2, CC2, CCSD, and CC3," *The Journal of Chemical Physics* **128**, 134110 (2008).

- ¹⁹M. L. Vidal, P. Pokhilko, A. I. Krylov, and S. Coriani, "Equation-of-motion coupled-cluster theory to model l-edge x-ray absorption and photoelectron spectra," *J. Phys. Chem. Lett.* **11**, 8314–8321 (2020).
- ²⁰J. P. Coe and M. J. Paterson, "Multireference x-ray emission and absorption spectroscopy calculations from monte carlo configuration interaction," *Theoretical Chemistry Accounts* **134**, 58 (2015).
- ²¹T. Fransson, I. E. Brumboiu, M. L. Vidal, P. Norman, S. Coriani, and A. Dreuw, "XABOOM: An x-ray absorption benchmark of organic molecules based on carbon, nitrogen, and oxygen 1s \rightarrow π^* transitions," *Journal of Chemical Theory and Computation* **17**, 1618–1637 (2021).
- ²²J. M. Kasper, T. F. Stetina, A. J. Jenkins, and X. Li, "Ab initio methods for l-edge x-ray absorption spectroscopy," *Chemical Physics Reviews* **1**, 011304 (2020).
- ²³L. Konecny, J. Vicha, S. Komorovsky, K. Ruud, and M. Repisky, "Accurate x-ray absorption spectra near l- and m-edges from relativistic four-component damped response time-dependent density functional theory," *Inorganic Chemistry* **61**, 830–846 (2022).
- ²⁴D. Prendergast and G. Galli, "X-ray absorption spectra of water from first principles calculations," *Physical Review Letters* **96**, 215502 (2006).
- ²⁵L. Triguero, O. Plashkevych, L. G. M. Pettersson, and H. Ågren, "Separate state vs. transition state Kohn-Sham calculations of X-ray photoelectron binding energies and chemical shifts," *J. Electron Spectrosc. Relat. Phenom.* **104**, 195–207 (1999).
- ²⁶M. P. Ljungberg, J. J. Mortensen, and L. G. M. Pettersson, "An implementation of core level spectroscopies in a real space projector augmented wave density functional theory code," *Journal of Electron Spectroscopy and Related Phenomena* **184**, 427–439 (2011).
- ²⁷G. S. Michelitsch and K. Reuter, "Efficient simulation of near-edge x-ray absorption fine structure (NEXAFS) in density-functional theory: Comparison of core-level constraining approaches," *The Journal of Chemical Physics* **150**, 074104 (2019).
- ²⁸A. J. Morris, R. J. Nicholls, C. J. Pickard, and J. R. Yates, "OptaDOS - a new tool for EELS calculations," *Journal of Physics: Conference Series* **371**, 012062 (2012).
- ²⁹R. J. Nicholls, A. T. Murdock, J. Tsang, J. Britton, T. J. Pennycook, A. Koós, P. D. Nellist, N. Grobert, and J. R. Yates, "Probing the Bonding in Nitrogen-Doped Graphene Using Electron Energy Loss Spectroscopy," *ACS Nano* **7**, 7145–7150 (2013).
- ³⁰Q. M. Ramasse, C. R. Seabourne, D.-M. Kepaptsoglou, R. Zan, U. Bangert, and A. J. Scott, "Probing the bonding and electronic structure of single atom dopants in graphene with electron energy loss spectroscopy," *Nano Letters* **13**, 4989–4995 (2013).
- ³¹T. P. Hardcastle, C. R. Seabourne, D. M. Kepaptsoglou, T. Susi, R. J. Nicholls, R. M. D. Brydson, A. J. Scott, and Q. M. Ramasse, "Robust theoretical modelling of core ionisation edges for quantitative electron energy loss spectroscopy of B- and N-doped graphene," *Journal of Physics: Condensed Matter* **29**, 225303 (2017).
- ³²H. Ikeno, F. M. F. de Groot, E. Stavitski, and I. Tanaka, "Multiplet calculations of l_{2,3} x-ray absorption near-edge structures for 3d transition-metal compounds," *Journal of Physics: Condensed Matter* **21**, 104208 (2009).
- ³³R. Laskowski and P. Blaha, "Understanding the $L_{2,3}$ x-ray absorption spectra of early 3d transition elements," *Physical Review B* **82**, 205104 (2010).
- ³⁴V. Begum-Hudde, T. Lojewski, N. Rothenbach, B. Eggert, A. Eschenlohr, K. Ollefs, M. E. Gruner, and R. Pentcheva, "Nature of excitons in the Ti/ and Ok edges of x-ray absorption spectra in bulk srTiO₃ from a combined first principles and many-body theory approach," *Phys. Rev. Res.* **5**, 013199 (2023).
- ³⁵M. Walter, H. Häkkinen, L. Lehtovaara, M. Puska, J. Enkovaara, C. Rostgaard, and J. J. Mortensen, "Time-dependent density-functional theory in the projector augmented-wave method," *The Journal of Chemical Physics* **128**, 244101 (2008).
- ³⁶R. C. Hilborn, "Einstein coefficients, cross sections, f values, dipole moments, and all that," *American Journal of Physics* **50**, 982–986 (1982).
- ³⁷M. Walter and H. Häkkinen, "Photoelectron spectra from first principles: from the many-body to the single-particle picture," *New Journal of Physics* **10**, 043018 (2008).
- ³⁸G. N. George, M. J. Hackett, M. Sansone, M. L. Gorbaty, S. R. Kelemen, R. C. Prince, H. H. Harris, and I. J. Pickering, "Long-range chemical sensitivity in the sulfur k-edge x-ray absorption spectra of substituted thiophenes," *The Journal of Physical Chemistry A* **118**, 7796–7802 (2014).
- ³⁹R. J. Cave, F. Zhang, N. T. Maitra, and K. Burke, "A dressed TDDFT treatment of the 2lag states of butadiene and hexatriene," *Chemical Physics Letters* **389**, 39–42 (2004).
- ⁴⁰M.E. Casida and M. Huix-Rotllant, "Progress in time-dependent density-functional theory | annual review of physical chemistry," *Annual Review of Physical Chemistry* **63**, 287–323 (2012).
- ⁴¹M. Leetmaa, M. P. Ljungberg, A. Lyubartsev, A. Nilsson, and L. G. M. Pettersson, "Theoretical approximations to x-ray absorption spectroscopy of liquid water and ice," *Journal of Electron Spectroscopy and Related Phenomena Water and Hydrogen Bonds*, **177**, 135–157 (2010).
- ⁴²J. Kasper, P. J. Lestrangle, T. F. Stetina, and X. Li, "Modeling l_{2,3}-edge x-ray absorption spectroscopy with real-time exact two-component relativistic time-dependent density functional theory," *J. Chem. Theory Comput.* **14**, 1998–2006 (2018).
- ⁴³M. Walter, M. Moseler, and L. Pastewka, "Offset-corrected δ -kohnsham scheme for semiempirical prediction of absolute x-ray photoelectron energies in molecules and solids," *Physical Review B* **94**, 041112 (2016).
- ⁴⁴I. Dabo, A. Ferretti, N. Poilvert, Y. Li, N. Marzari, and M. Cococcioni, "Koopmans' condition for density-functional theory," *Physical Review B* **82**, 115121 (2010).
- ⁴⁵C. Rostgaard, K. W. Jacobsen, and K. S. Thygesen, "Fully self-consistent GW calculations for molecules," *Physical Review B* **81**, 085103 (2010).
- ⁴⁶M. Walter, M. Vogel, V. Zamudio-Bayer, R. Lindblad, T. Reichenbach, K. Hirsch, A. Langenberg, J. Rittmann, A. Kulesza, R. Mitrić, M. Moseler, T. Möller, B. v. Issendorff, and J. Tobias Lau, "Experimental and theoretical 2p core-level spectra of size-selected gas-phase aluminum and silicon cluster cations: chemical shifts, geometric structure, and coordination-dependent screening," *Physical Chemistry Chemical Physics* **21**, 6651–6661 (2019).
- ⁴⁷M. Walter, F. Mangolini, J. B. McClimon, R. W. Carpick, and M. Moseler, "Fermi level pinning by defects can explain the large reported carbon 1s binding energy variations in diamond," (2019), arXiv:1902.02958 [cond-mat.mtrl-sci].
- ⁴⁸M. Walter, F. Mangolini, J. B. McClimon, R. W. Carpick, and M. Moseler, "Origin of c(1s) binding energy shifts in amorphous carbon materials," *Phys. Rev. Mater.* **9**, 035601 (2025).
- ⁴⁹T. Susi, D. J. Mowbray, M. P. Ljungberg, and P. Ayala, "Calculation of the graphene c 1s core level binding energy," *Physical Review B* **91**, 081401 (2015).
- ⁵⁰J. M. Kahk and J. Lischner, "Accurate absolute core-electron binding energies of molecules, solids, and surfaces from first-principles calculations," *Physical Review Materials* **3**, 100801 (2019).
- ⁵¹C. R. Jacob and M. Reiher, "Spin in density-functional theory," *International Journal of Quantum Chemistry* **112**, 3661–3684 (2012).
- ⁵²M. D. Manyakin, S. I. Kurganskii, O. I. Dubrovskii, O. A. Chuvchenkova, E. P. Domashevskaya, S. V. Ryabtsev, R. Ovsyannikov, E. V. Parinova, V. Sivakov, and S. Y. Turishchev, "Electronic and atomic structure studies of tin oxide layers using x-ray absorption near edge structure spectroscopy data modelling," *Materials Science in Semiconductor Processing* **99**, 28–33 (2019).
- ⁵³A. V. Ivanov, G. Levi, E. o. Jónsson, and H. Jónsson, "Method for calculating excited electronic states using density functionals and direct orbital optimization with real space grid or plane-wave basis set," *Journal of Chemical Theory and Computation* **17**, 5034–5049 (2021).
- ⁵⁴T. Susi, M. Kaukonen, P. Havu, M. P. Ljungberg, P. Ayala, and E. I. Kauppinen, "Core level binding energies of functionalized and defective graphene," *Beilstein Journal of Nanotechnology* **5**, 121–132 (2014).
- ⁵⁵T. A. Pascal, K. H. Wujcik, J. Velasco-Velez, C. Wu, A. A. Teran, M. Kapilashrami, J. Cabana, J. Guo, M. Salmeron, N. Balsara, and D. Prendergast, "X-ray absorption spectra of dissolved polysulfides in lithium-sulfur batteries from first-principles," *The Journal of Physical Chemistry Letters* **5**, 1547–1551 (2014).
- ⁵⁶P. E. Blöchl, "Projector augmented-wave method," *Physical Review B* **50**, 17953–17979 (1994).
- ⁵⁷J. J. Mortensen, L. B. Hansen, and K. W. Jacobsen, "Real-space grid implementation of the projector augmented wave method," *Physical Review B* **71**, 035109 (2005).
- ⁵⁸J. Enkovaara, C. Rostgaard, J. J. Mortensen, J. Chen, M. Duřak, L. Ferrighi, J. Gavnholt, C. Glinsvad, V. Haikola, H. A. Hansen, H. H. Kristof-

- fersen, M. Kuisma, A. H. Larsen, L. Lehtovaara, M. Ljungberg, O. Lopez-Acevedo, P. G. Moses, J. Ojanen, T. Olsen, V. Petzold, N. A. Romero, J. Stausholm-Møller, M. Strange, G. A. Tritsarlis, M. Vanin, M. Walter, B. Hammer, H. Häkkinen, G. K. H. Madsen, R. M. Nieminen, J. K. Nørskov, M. Puska, T. T. Rantala, J. Schiøtz, K. S. Thygesen, and K. W. Jacobsen, "Electronic structure calculations with GPAW: a real-space implementation of the projector augmented-wave method," *Journal of Physics: Condensed Matter* **22**, 253202 (2010).
- ⁵⁹J. J. Mortensen, A. H. Larsen, M. Kuisma, A. V. Ivanov, A. Taghizadeh, A. Peterson, A. Haldar, A. O. Dohn, C. SchÄfer, E. Ö. Jonsson, E. D. Hermes, F. A. Nilsson, G. Kastlunger, G. Levi, H. Jonsson, H. Häkkinen, J. Fojt, J. Kangsabanik, J. Sødequist, J. Lehtomäki, J. Heske, J. Enkovaara, K. T. Winther, M. Dulak, M. M. Melander, M. Ovesen, M. Louhivuori, M. Walter, M. Gjerding, O. Lopez-Acevedo, P. Erhart, R. Warmbier, R. Würdemann, S. Kaappa, S. Latini, T. M. Boland, T. Bliigaard, T. Skovhus, T. Susi, T. Maxson, T. Rossi, X. Chen, Y. L. A. Schmerwitz, J. Schiøtz, T. Olsen, K. W. Jacobsen, and K. S. Thygesen, "GPAW: An open python package for electronic structure calculations," *The Journal of Chemical Physics* **160**, 092503 (2024).
- ⁶⁰J. P. Perdew, K. Burke, and M. Ernzerhof, "Generalized gradient approximation made simple," *Physical Review Letters* **77**, 3865–3868 (1996).
- ⁶¹T. Olsen, "Designing in-plane heterostructures of quantum spin hall insulators from first principles: $1T' - \text{MoS}_2$ with adsorbates," *Phys. Rev. B* **94**, 235106 (2016).
- ⁶²O. Travnikova, K. J. Børve, M. Patanen, J. Söderström, C. Miron, L. J. Sæthre, N. Mårtensson, and S. Svensson, "The ESCA molecule—historical remarks and new results," *Journal of Electron Spectroscopy and Related Phenomena Special Issue in honor of Prof. T. Darrah Thomas: High-Resolution Spectroscopy of Isolated Species*, **185**, 191–197 (2012).
- ⁶³A. Wen and A. Hitchcock, "Inner shell spectroscopy of $(\eta^5\text{-c}_5\text{h}_5)_2\text{TiCl}_2$, $(\eta^5\text{-c}_5\text{h}_5)\text{TiCl}_3$, and TiCl_4 ," *Canadian Journal of Chemistry* **71**, 1632–1644 (1993).
- ⁶⁴M. Stener, G. Fronzoni, and M. de Simone, "Time dependent density functional theory of core electrons excitations," *Chemical Physics Letters* **373**, 115–123 (2003).
- ⁶⁵A.-N. Spiess and N. Neumeier, "An evaluation of r_2 as an inadequate measure for nonlinear models in pharmacological and biochemical research: a monte carlo approach," *BMC Pharmacology* **10** (2010).
- ⁶⁶S. P. Gleason, D. Lu, and J. Ciston, "Prediction of the Cu oxidation state from eels and xas spectra using supervised machine learning," *npj Computational Materials* **10** (2024).
- ⁶⁷A. A. Guda, S. A. Guda, A. Martini, A. N. Kravtsova, A. Algasov, A. Bugaev, S. P. Kubrin, L. V. Guda, P. Šot, J. A. van Bokhoven, C. Copéret, and A. V. Soldatov, "Understanding x-ray absorption spectra by means of descriptors and machine learning algorithms," *npj Computational Materials* **7** (2021).
- ⁶⁸A. A. Krasnoperova, E. S. Gluskin, L. N. Mazalov, and V. A. Kochubei, "The fine structure of the III, III absorption edge of sulfur in the SO_2 molecule," *Journal of Structural Chemistry* **17**, 947–950 (1976).
- ⁶⁹F. de Groot, "Multiplet effects in x-ray spectroscopy," *Coordination Chemistry Reviews* **249**, 31–63 (2005).
- ⁷⁰O. Baseggio, D. Toffoli, M. Stener, G. Fronzoni, M. de Simone, C. Grazioli, M. Coreno, A. Guarnaccio, A. Santagata, and M. D'Auria, "S2p core level spectroscopy of short chain oligothiophenes," *The Journal of Chemical Physics* **147**, 244301 (2017).
- ⁷¹O. Stauffert, S. Izadnia, F. Stienkemeier, and M. Walter, "Optical signatures of pentacene in soft rare-gas environments," *The Journal of Chemical Physics* **150**, 244703 (2019).
- ⁷²M. Walter and M. Moseler, "Ab initio wavelength-dependent raman spectra: Placzek approximation and beyond," *Journal of Chemical Theory and Computation* **16**, 576–586 (2020).
- ⁷³R. Puttner, M. Domke, D. Lentz, and G. Kaindl, "Si 2p photoabsorption in SiH_4 and SiCl_4 : molecular distortion in core-excited silane," *Physical Review A* **56**, 1228–1239 (1997).
- ⁷⁴J. Bozek, K. Tan, G. Bancroft, and J. Tse, "High resolution gas phase photoabsorption spectra of SiCl_4 and $\text{Si}(\text{CH}_3)_4$ at the silicon L edges: characterization and assignment of resonances," *Chemical Physics Letters* **138**, 33–42 (1987).
- ⁷⁵F. M. F. de Groot, M. O. Figueiredo, M. J. Basto, M. Abbate, H. Petersen, and J. C. Fuggle, "2p x-ray absorption of titanium in minerals," *Physics and Chemistry of Minerals* **19**, 140–147 (1992).
- ⁷⁶R. Ruus, A. Kikas, A. Saar, A. Ausmees, E. Nõmmiste, J. Aarik, A. Aidla, T. Uustare, and I. Martinson, "Ti 2p and O 1s x-ray absorption of TiO_2 polymorphs," *Solid State Communications* **104**, 199–203 (1997).
- ⁷⁷A. Jain, S. P. Ong, G. Hautier, W. Chen, W. D. Richards, S. Dacek, S. Cholia, D. Gunter, D. Skinner, G. Ceder, and K. A. Persson, "Commentary: The Materials Project: A materials genome approach to accelerating materials innovation," *APL Materials* **1**, 011002 (2013).
- ⁷⁸K. van Benthem, C. Elsässer, and R. H. French, "Bulk electronic structure of SrTiO_3 : Experiment and theory," *Journal of Applied Physics* **90**, 6156–6164 (2001).
- ⁷⁹K. van Benthem, C. Elsässer, and M. Rühle, "Core-hole effect on the ELNES of SrTiO_3 : Experiment and theory," *Microscopy and Microanalysis* **9**, 68–69 (2003).
- ⁸⁰K. van Benthem, C. Elsässer, and M. Rühle, "Core-hole effects on the ELNES of absorption edges in SrTiO_3 ," *Ultramicroscopy Proceedings of the International Workshop on Strategies and Advances in Atomic Level Spectroscopy and Analysis*, **96**, 509–522 (2003).
- ⁸¹M. Hepting, D. Li, C. J. Jia, H. Lu, E. Paris, Y. Tseng, X. Feng, M. Osada, E. Been, Y. Hikita, Y.-D. Chuang, Z. Hussain, K. J. Zhou, A. Nag, M. Garcia-Fernandez, M. Rossi, H. Y. Huang, D. J. Huang, Z. X. Shen, T. Schmitt, H. Y. Hwang, B. Moritz, J. Zaanen, T. P. Devereaux, and W. S. Lee, "Electronic structure of the parent compound of superconducting infinite-layer nickelates," *Nature Materials* **19**, 381–385 (2020).
- ⁸²M. Finazzi, N. B. Brookes, and F. M. F. de Groot, " $2p_{3/2}$, $2p_{3/2}$, and $2p_{3/2}$ resonant Auger spectroscopy from NiO ," *Physical Review B* **59**, 9933–9942 (1999).
- ⁸³T. Moriyama, K. Oda, T. Ohkuchi, M. Kimata, and T. Ono, "Spin torque control of antiferromagnetic moments in NiO ," *Scientific Reports* **8**, 14167 (2018).
- ⁸⁴O. A. Chuvankova, S. V. Boikov, N. I. Ryabtsev, E. V. Parinova, R. G. Chumakov, A. M. Lebedev, D. Smirnov, A. Makarova, S. S. Titova, K. A. Fateev, and S. Y. Turishchev, "Electronic structure and composition of tin oxide thin epitaxial and magnetron layers according to synchrotron xanes studies," *Kondensirovannye Sredy I Mezhfaznye Granitsy = Condensed Matter and Interphases* **26**, 153–160 (2024).
- ⁸⁵M. Batzill and U. Diebold, "The surface and materials science of tin oxide," *Progress in Surface Science* **79**, 47–154 (2005).
- ⁸⁶G. Yang, L. Li, W. B. Lee, and M. C. Ng, "Structure of graphene and its disorders: a review," *Science and Technology of Advanced Materials* **19**, 613–648 (2018).